

Proton and deuteron production in neutron-induced reactions on carbon at $E_n = 42.5, 62.7, \text{ and } 72.8 \text{ MeV}$

I. Slypen,* V. Corcalciuc, and J. P. Meulders

*Institut de Physique Nucléaire, Université Catholique de Louvain,
Chemin du Cyclotron 2, B-1348 Louvain-la-Neuve, Belgium*

(Received 13 June 1994)

Double-differential cross sections for proton and deuteron production in fast neutron-induced reactions on carbon are reported for three incident neutron energies: 42.5, 62.7, and 72.8 MeV. Angular distributions were measured at laboratory angles between 20° and 160° . Procedures for data taking and data reduction are presented. Energy-differential cross sections and total cross sections are also reported. Experimental cross sections are compared with existing data and with theoretical calculations in the frame of the intranuclear cascade model.

PACS number(s): 28.20.-v, 25.40.Hs

I. INTRODUCTION

Experimental measurements of charged particle production for fast neutron-induced reactions in the incident energy range 30–80 MeV are rather scarce [1]. Nevertheless, a wealth of information can be obtained about nuclear mechanisms and nuclear structure of the involved nuclei. Besides, in the case of light target nuclei, a detailed knowledge of cross sections helps to evaluate the contribution of a given element as a constituent of human tissue or neutron detector [2,3].

We report here double-differential cross sections for proton and deuteron production from carbon at 42.5, 62.7, and 72.8 MeV incident neutron energies. Measurements were done at laboratory angles between 20° and 160° .

In Sec. II, the experimental setup is briefly described. Data reduction procedures including normalization and corrections to the measured spectra are presented in Sec. III. Experimental results and theoretical calculations are shown in Sec. IV. Conclusions are covered in Sec. V.

II. EXPERIMENTAL SETUP

The fast neutron beam facility existing at the Louvain-la-Neuve Cyclotron, CYCLONE, has been previously described in detail [4–6]. The accelerated proton beam is focused on a natural lithium target. The ${}^7\text{Li}(p, n){}^7\text{Be}_{g.s.}$ ($Q = -1.644 \text{ MeV}$) and ${}^7\text{Li}(p, n){}^7\text{Be}^*$ (0.431 MeV) reactions produce at 0° laboratory angle a quasimonochromatic neutron beam [7]. Using a 3-mm-thick lithium target and a 10^{-5} A proton beam, about 10^6 n/s are available at the location of our reaction chamber (around 3 m downstream from the lithium target). The neutron energy spectrum at 0° consists in a well-defined peak con-

taining about 50% of the neutrons plus a continuum of low-energy neutrons. Figure 1 shows a typical neutron spectrum for 45 MeV protons incident on a 3-mm-thick lithium target. It is reconstructed using the recoil proton spectrum from a 1-mm-thick polypropylene $(\text{C}_3\text{H}_6)_n$ target, after normalization with n - p cross sections [8]. The full width at half maximum is about 2 MeV, with an important contribution coming from the kinematics of the n - p scattering in the angular opening of the detector (2° – 3°).

The collimated neutron beam strikes the target located in our reaction chamber. Details of the neutron collimating system are given elsewhere [4–6]. We only mention that at the location of our target the neutron-beam radial distribution (beam profile), measured with a NE102 scintillator (5 mm in diameter), is as shown in the in-

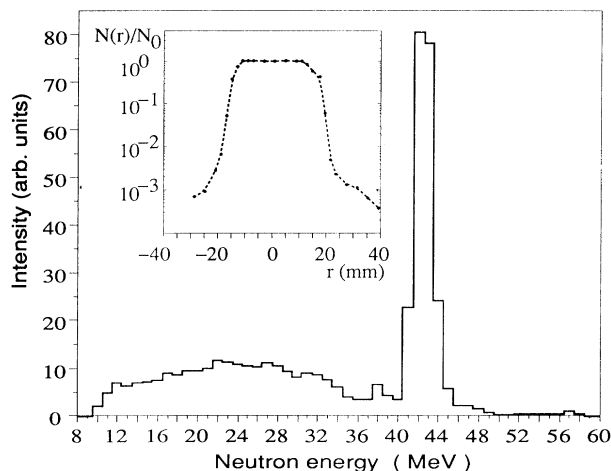


FIG. 1. Neutron spectrum resulting from a 45-MeV proton beam on a 3-mm-thick lithium target, reconstructed from n - p recoil protons. The inset shows the neutron beam profile (radial distribution) measured at 3 m downstream of the lithium target, normalized to the intensity in the center. The dashed curve serves to guide the eye.

*To whom correspondence should be addressed.

set in Fig. 1 and is in good agreement with previous measurements [4].

The evacuated reaction chamber (406 mm in diameter) is coupled to the exit of the neutron collimator. It can be turned in the reaction plane and has ten ports to accommodate the holding system of the telescopes. Angles from 20° to 160° in steps of 10° are available.

Four charged-particle detector telescopes are used simultaneously. Each of them consists of a ΔE detector (NE102 plastic scintillator, 0.1 mm thick, 4 cm in diameter) viewed by an XP2020 photomultiplier via a lucite light guide, and an E detector [CsI(Tl) crystal, 22 mm thick, 38.1 mm in diameter], viewed by an XP2262B photomultiplier. The E detector can stop 80-MeV protons. A coincidence is required between ΔE and E detectors in order to suppress an important part of the background present in such type of experiments.

An elemental carbon target ($5 \times 5 \text{ cm}^2$ surface and 1 mm thick) is used. The angle of the target with the beam was chosen to minimize the thickness of the target material traversed by the produced charged particles towards the telescopes.

The energy calibration of the detectors would ideally require to bring a direct charged particle beam to the reaction chamber, which is not easy in the present neutron facility. Therefore, the protons and deuterons recoiling from a polypropylene (1 or 0.5 mm thick) and a 0.6-mm-thick deuterated polypropylene target, respectively, are used. They are recorded at laboratory angles from 20° to 70° in steps of 10° , for each of the four telescopes and at each of the three incident neutron energies. Moreover, the n - p scattering is registered with good statistics, for a precise determination of a differential cross sections to be subsequently used as reference for the carbon measurement.

Charged-particle discrimination spectra are obtained in two ways: by using the energy information from E and ΔE detectors and by charge integration of the CsI light output pulse [9–11]. In the latter case, the signal is integrated during the fast gate (600 ns width) and a slow gate (2700 ns width). A combined use of the two separation methods [11,12] allows a very good separation of the reaction products over their entire energy range. This way, the background is well separated in a ΔE - E spectrum and therefore eliminated. Figure 2 shows a particle separation spectrum in slow vs fast component display, before [Fig. 2(a)] and after [Fig. 2(b)] the elimination of the background. Moreover, after the selection of a certain reaction product in Fig. 2(b), a ΔE - E redisplay of the selected events allows a further discrimination of an eventual contamination with other reaction products, mainly in the low-energy region.

The beam monitoring system is realized in two ways. Behind the lithium target, the incident proton beam is deflected by a magnetic dipole into a water-cooled Faraday cup which serves as a beam monitor. Downstream our reaction chamber, and coupled to it, there is a second evacuated chamber in which a 1-mm-thick polypropylene target is placed perpendicular to the neutron beam. A charged-particle telescope detects at 45° the $H(n, p)$ scattered protons. It consists of a NE102 (2-mm-thick) scin-

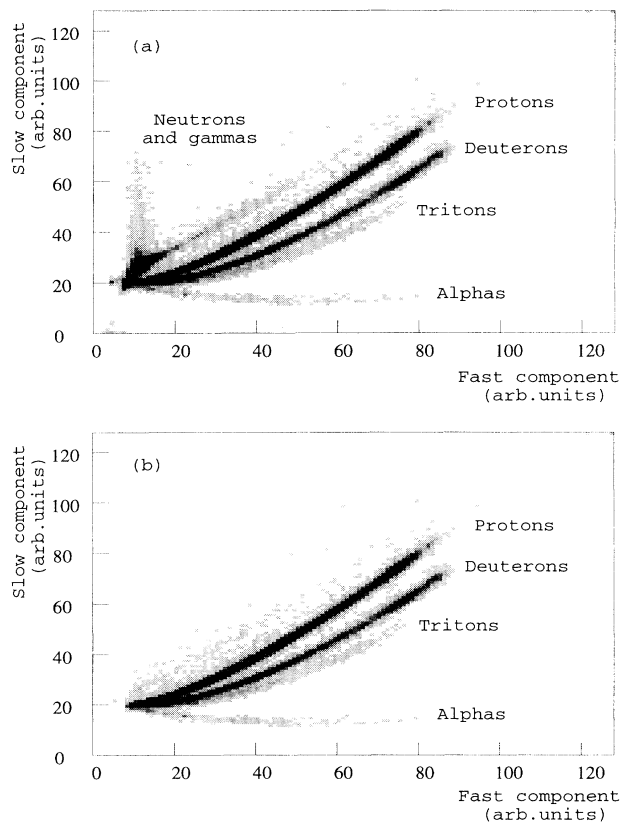


FIG. 2. Particle identification in two-dimensional spectra of slow vs fast component of the CsI light output response: (a) before background suppression and (b) after background suppression (see text).

tillator as ΔE and a CsI(Tl) crystal as E detector. The integral of the recoil proton peak serves as a second monitor during the measurements. The agreement between the two monitoring systems was very good during the data taking.

For each charged-particle event in the telescopes, a time of flight (TOF) between a capacitive beam pickoff located upstream of the neutron producing target and the ΔE detector is registered, and subsequently used to select only those events associated with the neutrons in the main neutron peak.

The acquisition system reads each event (a structured set of correlated words) and then packs them as data blocks of fixed size in a buffer system from where they can be accessed by different data processing programs. The programs can run on UNIX workstation connected to the VMEbus system through an Ethernet system [13]. Data can be archived on workstation disks and on Exabyte tapes for an off-line analysis.

III. DATA REDUCTION

We shall briefly describe the procedure adopted for data reduction. More details are given in Refs. [11,12].

Once a reaction product (proton or deuteron) is se-

lected in Fig. 2(b), by complementary use of ΔE - E and slow vs fast component in the particle discrimination spectra, a reliable selection of the desired events is obtained. Subsequently, using TOF information and knowing the involved flight distances and energies of the particles (from the energy calibration), a further selection is done of only those events induced by the neutrons from the monoenergetic peak. The statistics in our carbon measurements correspond to an acquisition time of 24 h for forward and 48 h for backward angles, with about 12×10^{-6} A mean proton beam on a 3-mm-thick lithium target.

Absolute cross sections are obtained by normalization to our measured $H(n,p)$ scattering cross sections. With each of the four telescopes, angular distributions for the n - p elastic scattering were measured at six laboratory angles between 20° and 70° . In order to have reliable differential cross sections, a good knowledge of the relative solid angles is necessary. Besides, for $H(n,p)$ scattering at higher laboratory angles, only a fraction of the target will produce protons with enough energy to overcome the energy loss in the target material and the ΔE detector, and the energy threshold of the E detector, in order to be registered by the telescope. Solid angles and thick target corrections are calculated by a Monte Carlo simulation program of the experiment [14]. The program includes energy losses in the target material and the ΔE detector, the threshold of E detectors, kinematics of the reaction, neutron beam energy width (Fig. 1), neutron beam profile (see inset in Fig. 1), target-detector geometry, and geometry of the collimating system of the telescopes [14]. The average angular opening of the collimating system for the detection of charged particle products is 2° - 3° and the neutron beam energy width is about 2 MeV. This way, for each of the telescopes, six normalization points are available, covering a large energy range, and the normalization factor was a mean value of them. Generally, the spread of these values around the mean value was less than 3%.

The rather thick carbon target, the 0.1-mm-thick ΔE detector used, and the threshold of the E detector will limit the registration of the low-energy charged-particle products to only fractions of the entire target thickness; therefore, the spectra should be accordingly corrected. These effects are taken into account by using the above-mentioned simulation program. The calculated correction factors are mean values over the energy spread introduced by the target material and ΔE detector, for each of the charged particle products. For our carbon target and the specified characteristics of ΔE - E telescopes, these corrections start from around, respectively, 12-MeV proton and 19-MeV deuteron energy downwards to, respectively, 5-MeV proton and 9–10-MeV deuteron energy cutoffs in the spectra. These limits are influenced by the target-telescope relative angle [14].

One may get indirect information about the energy dependence of the telescope efficiency vs energy of the detected charged particles. The neutron spectrum shown in Fig. 1 is obtained from $H(n,p)$ scattered protons at 40° after normalization of the $\sigma_{(n,p)}(40^\circ)$ cross section vs neutron energy, from the parametrization of Ref. [8].

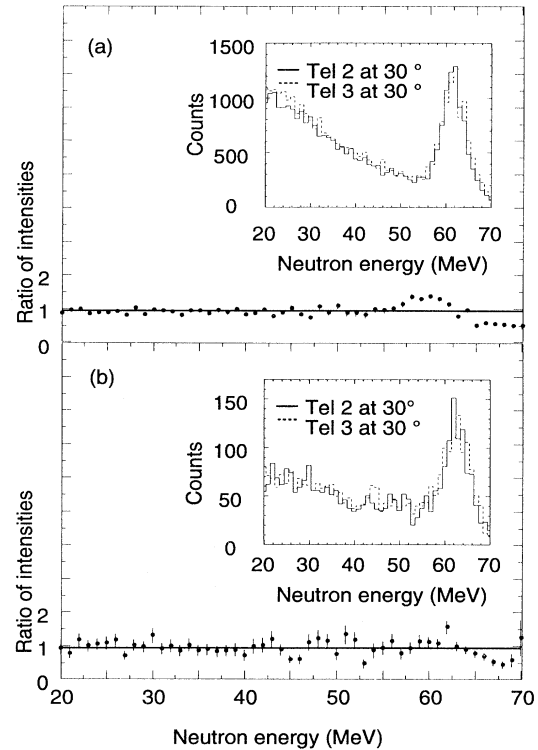


FIG. 3. Ratio of reconstructed incident neutron beam deduced: (a) from $H(n,p)$ with different telescopes at the same angle and (b) from (n,d) on the deuterated polypropylene target, with different telescopes at the same laboratory angle. In the insets are shown superposition of reconstructed neutron spectra from which the ratio was obtained.

The neutron spectrum in Fig. 1 must be invariant for all our measurements at 45-MeV incident proton energy on the lithium target.

Figure 3(a) shows in the inset superposed reconstructed [from $H(n,p)$ scattering] incident neutron energy spectra as histograms in steps of 1 MeV. They are obtained from 65-MeV incident proton energy data for two different telescopes at the same laboratory angle. The ratio of the two spectra has a constant value over a wide neutron (therefore proton) energy range. After solid angle corrections, this constant becomes nearly one, as shown in the figure. A similar results is shown in Fig. 3(b), but this time the reconstructed neutron spectra are obtained from (n,d) scattering, by using the deuterated polypropylene target. In fact, the ratios shown in Fig. 3 are merely the ratios of the efficiencies of the two telescopes. As the thresholds of the telescopes are different, one might conclude that the efficiency of each telescope is constant, within the experimental errors, over a wide energy range of the detected charged particles. The scattering of the ratio in the region of the main peak is due to slightly different widths of these peaks in different telescopes, for which no corrections were done. Similar results are obtained for the four telescopes used and all the measured scattering angles. For the neutron spectra in the insets of Fig. 3, no normalization with the respective

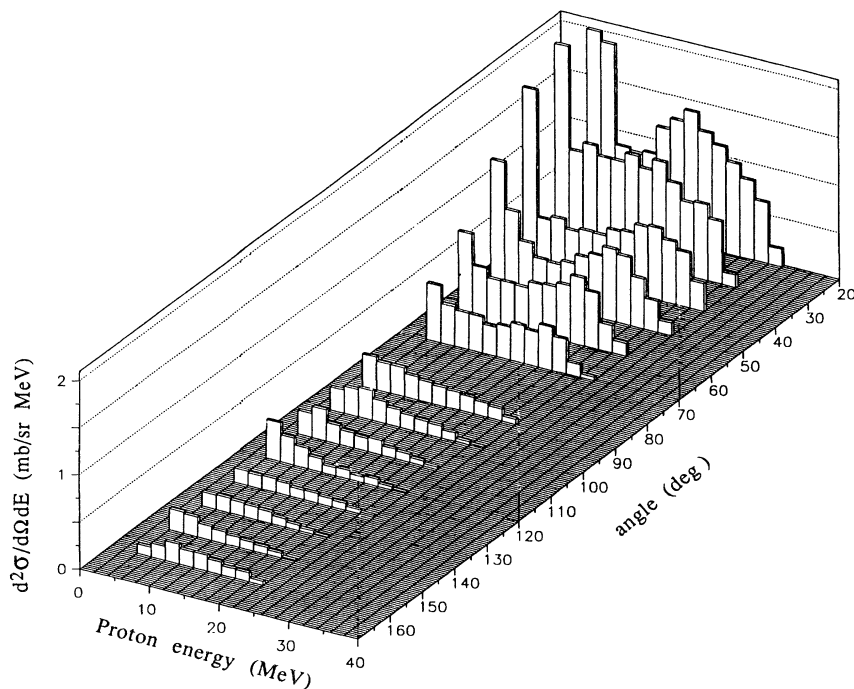


FIG. 4. Angular distribution of final double-differential cross sections for $^{12}\text{C}(n, px)$ reaction at 14 laboratory angles (histograms in steps of 2 MeV) for 42.5-MeV incident neutron energy.

(n, p) scattering cross sections vs neutron energy is necessary, because they are selected at the same laboratory angle.

IV. RESULTS AND DISCUSSION

Using the procedures outlined above, final double-differential cross sections for proton and deuteron pro-

duction were obtained for three incident neutron energies corresponding to the main neutron peak: 42.5, 62.7, and 72.8 MeV, resulting respectively from 45, 65, and 75 MeV incident proton energy on the lithium target. Figures 4–9 show in a three-dimensional (3D) representation the complete measured angular distributions of proton and deuteron energy spectra for, respectively, 42.5, 62.7, and 72.8 MeV incident neutron energy. The measured cross sections are represented as histograms in steps of 2 MeV.

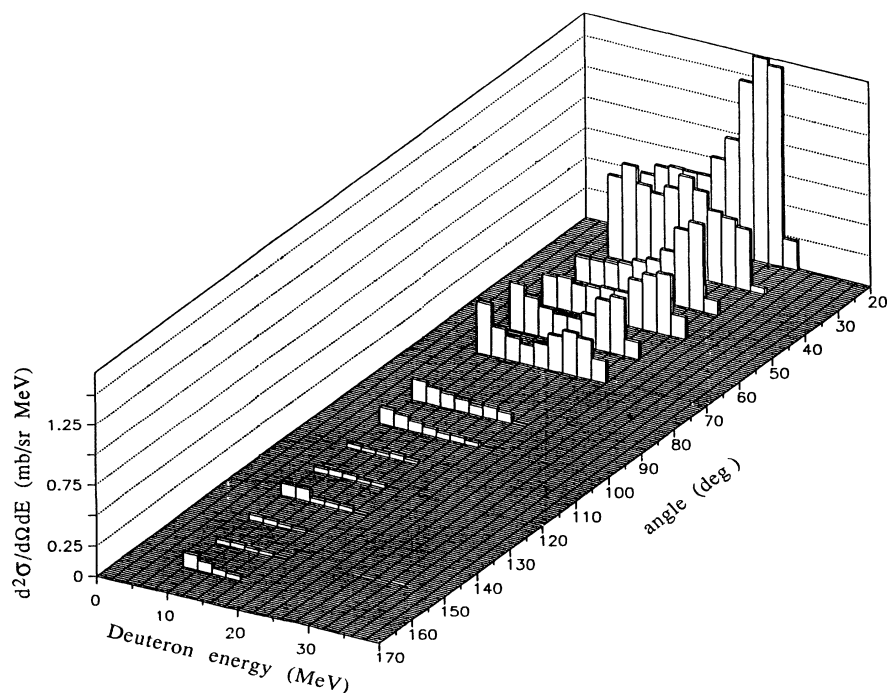


FIG. 5. Same as in Fig. 4 for the case of $^{12}\text{C}(n, dx)$ reaction.

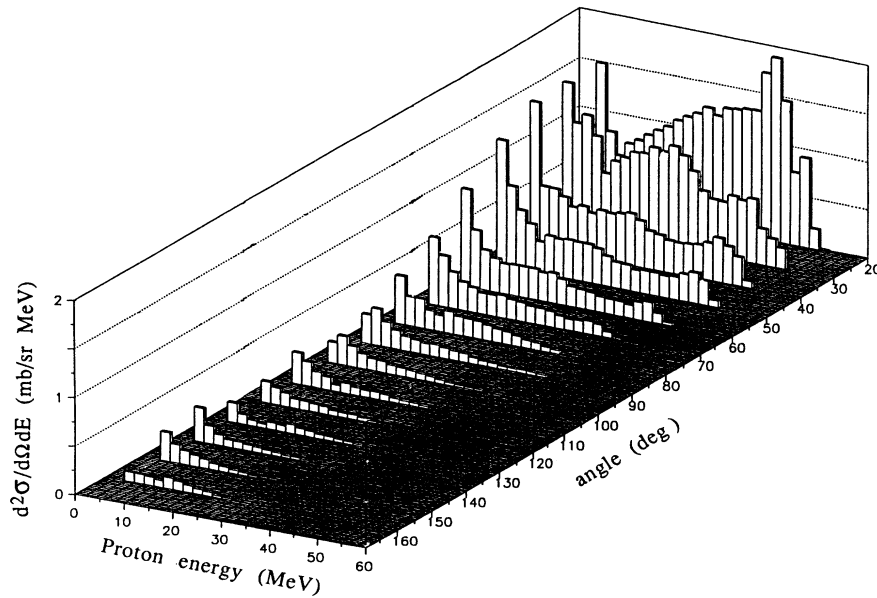


FIG. 6. Angular distribution of final double-differential cross sections for $^{12}\text{C}(n, px)$ reaction at 15 laboratory angles (histograms in steps of 2 MeV) for 62.7-MeV incident neutron energy.

The horizontal scale gives the energy of the charged particle produced in the reaction. Low-energy cuts are, respectively, around 5 MeV for protons and 9–10 MeV for deuterons, mainly given by the thickness of the ΔE detector and the energy threshold of the E detector (about 1.5 MeV).

The overall relative errors of the points in the spectra are about 5%, except for low-energy parts where they can be larger as a result of the thick target correction procedure [14]. The uncertainty of the cross-section absolute scale is less than 6% given by errors in the measured reference (n, p) cross sections (5%), beam monitoring (2%), statistics in the $\text{H}(n, p)$ recoil proton peak (2%), solid-angle corrections (1%), and number of target nuclei (1%).

The angular distributions in Figs. 4–9 show a strong

peaking at forward laboratory angles for both protons and deuterons. Nevertheless, the deuteron angular distribution at 42.5 MeV is less steep than the corresponding one at 62.7 MeV. The 72.8-MeV data are very similar, in both shape and magnitude, to the 62.7-MeV ones.

Figures 10–13 show double-differential cross sections for the $^{12}\text{C}(n, px)$ and $^{12}\text{C}(n, dx)$ reactions at several laboratory angles for, respectively, 42.5- and 62.7-MeV incident neutron energy (note the change of scale from one angle to another). The present data are shown as open dots with their respective errors and the corresponding (dotted line) histograms. For comparison the data of Ref. [15] are also presented (triangles). The solid line histograms are calculated cross sections of Ref. [16] for, respectively, 40- and 60-MeV incident neutrons. The cal-

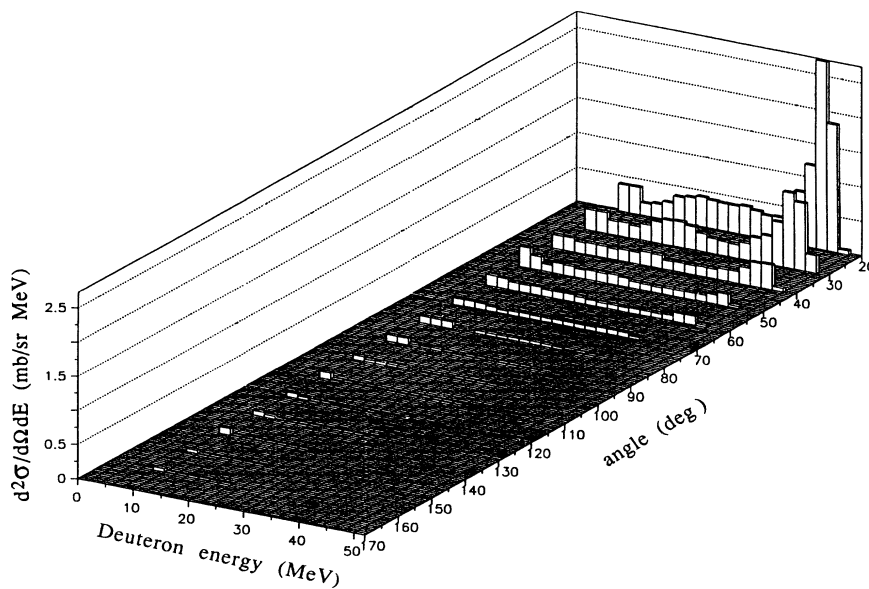


FIG. 7. Same as in Fig. 6 for the case of $^{12}\text{C}(n, dx)$ reaction.

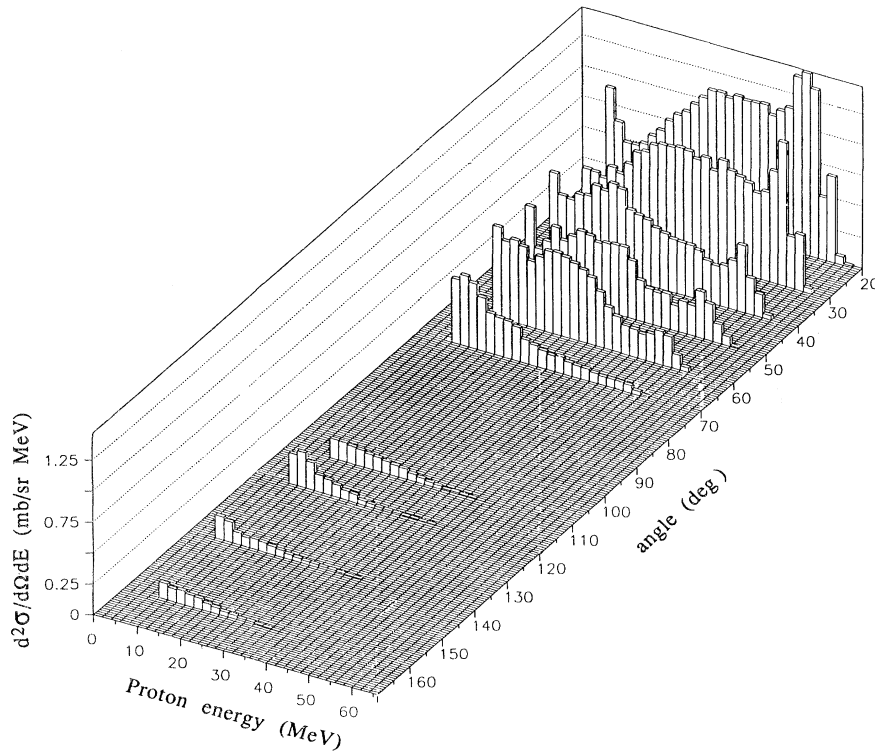


FIG. 8. Angular distribution of final double-differential cross sections for $^{12}\text{C}(n, px)$ reaction at 10 laboratory angles (histograms in steps of 2 MeV) for 72.8-MeV incident neutron energy.

culations are done with an intranuclear cascade model code (INCA) [16–18]. It includes alpha clustering and particle pickup, followed by Fermi breakup mechanism incorporating decay via intermediate particle-unstable states [16]. The processes responsible for the prominent structure at forward angles for the high-energy protons or

high-energy deuterons peak are not included in the calculations of Ref. [16]. The peaks for the three discrete states in proton spectra (ground state, 4.4, and 7.9 MeV) [11,19,20] as well as the main deuteron peak, have been separately analyzed.

Within the experimental errors, our 42.5-MeV data

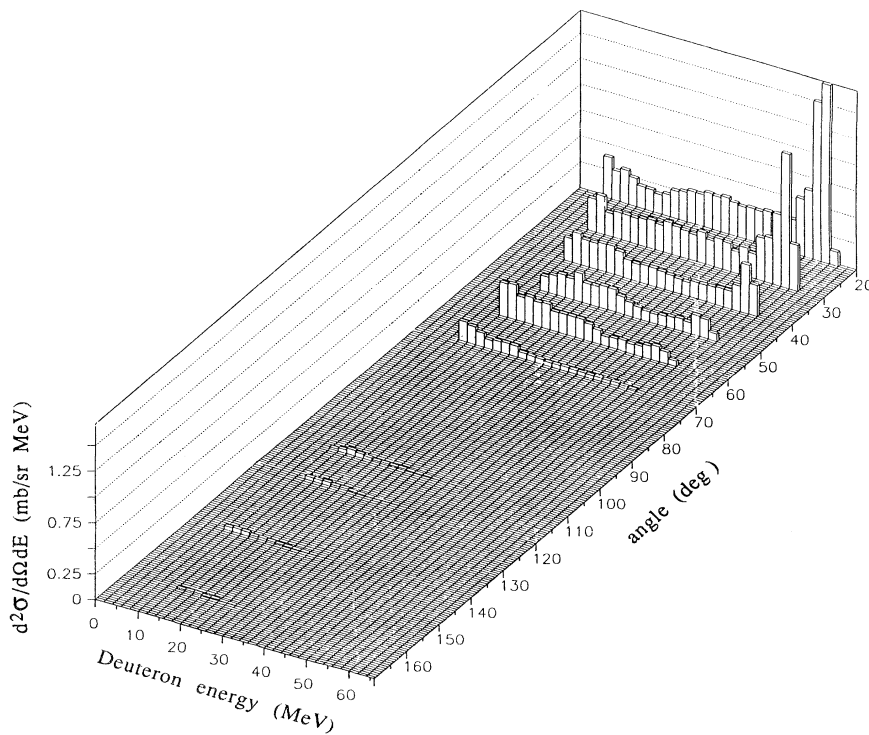


FIG. 9. Same as in Fig. 8 for the case of $^{12}\text{C}(n, dx)$ reaction.

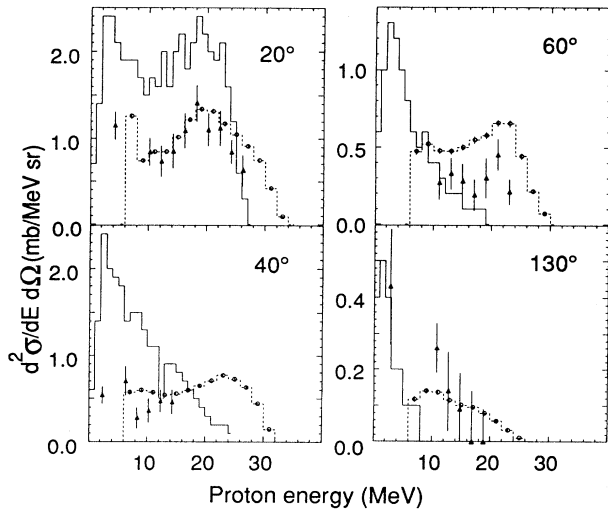


FIG. 10. Measured double-differential cross sections at several laboratory angles (open dots in steps of 2 MeV and dotted histograms) for $^{12}\text{C}(n, px)$ reactions at 42.5-MeV incident neutron energy. Corresponding data of Ref. [15], at 39.7 MeV, are shown as triangles. Our 60° data are compared with 65° data of Ref. [15]. Calculations for 40-MeV neutron energy from Ref. [16] are presented as continuous line histograms in steps of 2 MeV.

(Figs. 10 and 11) are in fair agreement with 39.7-MeV data of Ref. [15] particularly at forward angles. Unfortunately the polystyrene $(\text{CH})_n$ target used in Ref. [15] for carbon measurements, introduces gaps in the proton spectra (40° and 60° laboratory angle) which limit the energy range for a meaningful comparison. The present data at 62.7 MeV compare well, within the experimental errors, with 60.7-MeV data of Ref. [15] (Figs. 12 and 13).

The theoretically calculated cross sections of Ref. [16] at 40 MeV are rather far from the 42.5-MeV experimental values for protons, giving nevertheless a better descrip-

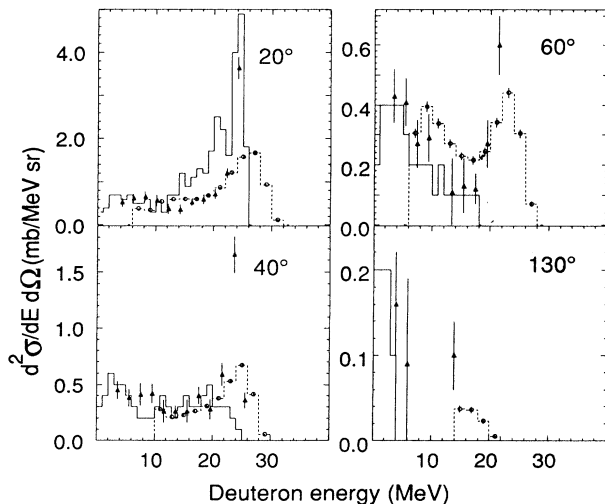


FIG. 11. Same as in Fig. 10 for the case of deuterons.

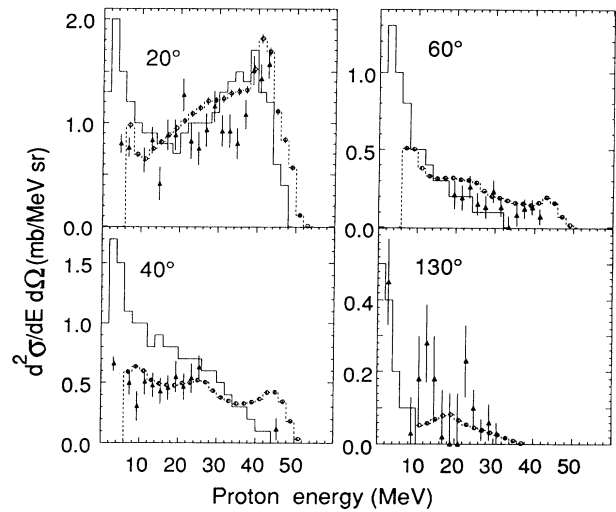


FIG. 12. Measured double-differential cross sections at several laboratory angles (open dots in steps of 2 MeV and dotted histograms) for $^{12}\text{C}(n, px)$ reactions at 62.7-MeV incident neutron energy. Corresponding data of Ref. [15], at 60.7 MeV are shown as triangles. Our 60° data are compared with 65° data of Ref. [15]. Calculations for 60-MeV neutron energy from Ref. [16] are presented as continuous line histograms in steps of 2 MeV.

tion of deuteron spectra. The theoretical calculations at 60-MeV incident neutron energy are in a better agreement with our 62.7-MeV experimental data both for the shape and the magnitude of the cross sections (Figs. 12 and 13). Generally, the theory predicts less high-energy charged particles than experimentally observed [15].

Energy-differential cross sections are presented (histograms of 2-MeV steps) in Figs. 14 and 15 for protons and deuterons for the reported three incident neutron energies. They are obtained by the solid-angle integration of the data shown in Figs. 4–9. The measured angu-

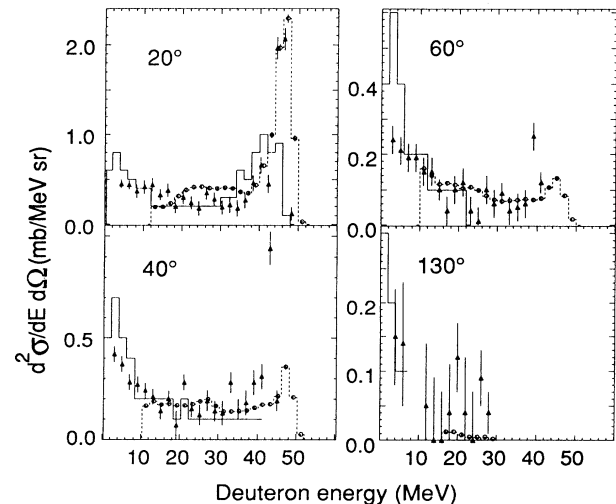


FIG. 13. Same as in Fig. 12 for the case of deuterons.

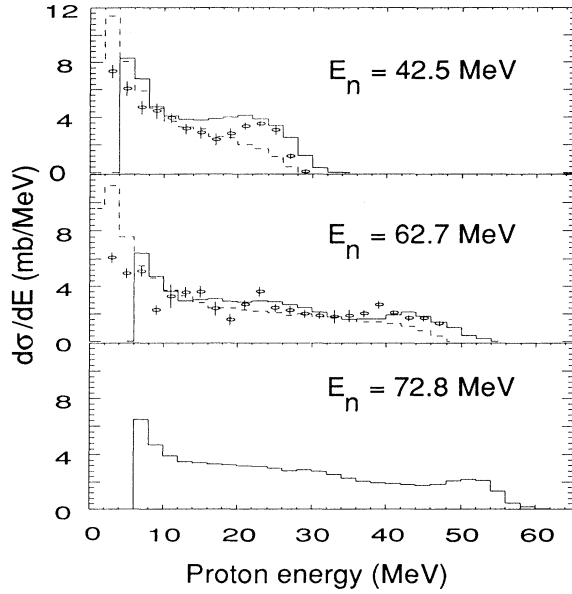


FIG. 14. Energy-differential cross sections for proton production at the three incident neutron energies represented as solid line histograms in steps of 2 MeV. Dotted line histograms correspond to calculations at, respectively, 40- and 60-MeV incident neutron energy from Ref. [16]. The open dots represent experimental results of Ref. [15] at, respectively, 39.7- and 60.7-MeV incident neutron energy.

lar distributions were completed with theoretically calculated cross sections of Ref. [16] for very forward (2.5° and 10°) and very backward (170° and 177.5°) angles. Nevertheless, their contribution is small, due to the multiplication with $\sin\theta$ in the angle integration. The dotted line histograms in Figs. 14 and 15 are calculated energy-

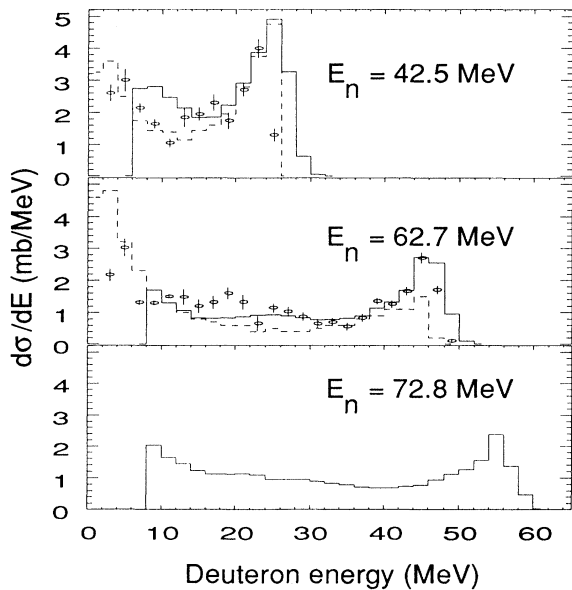


FIG. 15. Same as in Fig. 14 for the case of deuterons.

TABLE I. Total cross sections for proton and deuteron production induced by neutrons of 42.5, 62.7, and 72.8 MeV on carbon. Theoretical values are also shown for comparison.

E_n (MeV)	$\sigma(n, px)$ (mb)	Errors (mb)	$\sigma(n, dx)$ (mb)	Errors (mb)	Reference
42.5	149.0	± 10	82.3	± 6	This work
40.0	116.6		62.7		[16]
62.7	173.2	± 13	79.3	± 6	This work
60.0	150.6		60.7		[16]
72.8	198.6	± 14	87.6	± 6	This work

differential cross sections of Ref. [16] for, respectively, 40- and 60-MeV incident neutron energies. It is interesting to note in the case of deuterons (Fig. 15) that, while the theory describes fairly well the high-energy peaking of the cross section for 42.5-MeV data, it explains less than half of the corresponding measured 62.7-MeV cross section. No theoretical calculations are available for 72.8-MeV measurements.

As most of the applications use the energy-differential cross sections, we show for comparison in Figs. 14 and 15 as open dots, also the corresponding values of Ref. [15] for 39.7- and 60.7-MeV incident neutron energy. The two experimental sets of data are in good agreement over a large energy range of the produced charged particles.

Table I gives total cross sections for proton and deuteron production resulting from the integration of the energy-differential cross sections in Figs. 14 and 15. Below the experimental energy cutoffs, the theoretical cross sections, shown in Figs. 14 and 15, are used. For 72.8 MeV the measurements are extrapolated with the cross-section values from calculations at 60 MeV from Ref. [16]. The estimated experimental errors indicated in Table I take in count a 10% error for the theoretical cross sections used to extrapolate below the experimental energy cutoffs.

Given as well in Table I are theoretical values of Ref. [16]. Generally, the fact that the measured cross sections are higher than the theoretical ones, results as mentioned above, from more high-energy particles measured in the energy spectra than theoretically predicted. Experimental values in Table I compare well with total proton and deuteron yields of, respectively, 172.5 ± 15 and 89.5 ± 10 mb, at 90-MeV incident neutron energy, from Ref. [21].

V. CONCLUSIONS

Proton and deuteron production energy spectra ($d^2\sigma/d\Omega dE$) resulting from the interaction of fast neutrons on carbon, are reported at three incident energies between 40 and 75 MeV. Measurements were done with good statistics at the fast neutron facility of the Louvain-la-Neuve Cyclotron. Angular distributions are measured at laboratory angles between 20° and 160° for 42.5 MeV (14 angles), 62.7 MeV (15 angles), and 72.8 MeV (10 angles) incident neutron energies.

The present data are overall in agreement with previous measurements (Ref. [15]) within the reported experimental errors and in energy range of the produced

charged particles where a meaningful comparison is possible. Experimental data are compared with intranuclear cascade model calculations of Ref. [16]. The agreement of the calculated and measured double-differential cross sections is good at forward angles for the 62.7-MeV data, both for the shape of the spectra and the absolute magnitude of the cross sections. For 42.5 MeV the theoretical predictions are less satisfactory. No calculations are available to compare with our 72.8-MeV data. Generally the theoretical calculations predict less high-energy protons and deuterons than experimentally measured, especially for backward angles.

Energy-differential cross sections are deduced from our measured double-differential cross sections. Overall, they compare rather well with previously reported data (Ref. [15]) and with theoretical calculations (Ref. [16]). The agreement of the theoretical calculations with the experimental energy-differential cross sections give some confidence in using calculations to extrapolate below the experimental low-energy cutoffs. By using these extrapola-

tions, complete energy-differential cross sections ($d\sigma/dE$) or angle-differential cross sections ($d\sigma/d\Omega$) may be obtained for a further use [light response of a neutron detector, KERMA (Kinetic Energy Released per Mass unit) factor calculation, etc.].

Only an illustrative selection of detailed results has been presented here. Complete double-differential production cross sections and their angular distributions may be obtained from I. Slypen. A paper concerning KERMA factors, deduced from the experimental data of this work, has been published [22].

ACKNOWLEDGMENTS

We would like to thank the Louvain-la-Neuve Cyclotron staff for permanent assistance and quality of the beam. We acknowledge support of the Institut Interuniversitaire des Sciences Nucléaires, Belgium, and partly the European Economic Community (Contract FI3P-93-0084-BE).

-
- [1] T. S. Subramanian, J. L. Romero, and F. P. Brady, *Nucl. Instrum. Methods* **174**, 475 (1980).
 - [2] A. H. Wells, *Radiat. Res.* **80**, 1 (1979).
 - [3] A. S. Meigooni, J. S. Petler, and R. W. Finlay, *Phys. Med. Biol.* **29**, 643 (1984).
 - [4] A. Bol, P. Leleux, P. Lipnik, P. Macq, and A. Ninane, *Nucl. Instrum. Methods Phys. Res.* **214**, 169 (1983).
 - [5] C. Dupont, P. Leleux, P. Lipnik, P. Macq, and A. Ninane, *Nucl. Instrum. Methods Phys. Res. Sect. A* **256**, 169 (1983).
 - [6] C. Dupont, Ph.D. thesis, Université Catholique de Louvain, 1987 (unpublished).
 - [7] J. A. Jungerman, F. P. Brady, W. J. Knox, T. Montgomery, M. R. McGie, J. L. Romero, and Y. Ishizaki, *Nucl. Instrum. Methods* **94**, 421 (1971).
 - [8] J. Binstock, *Phys. Rev. C* **10**, 19 (1974).
 - [9] F. Benrachi, B. Chambon, B. Cheynis, D. Drain, C. Pastor, D. Seghier, K. Zaid, A. Giorni, D. Heuer, A. Llères, C. Morand, P. Stassi, and J. B. Viano, *Nucl. Instrum. Methods Phys. Res. Sect. A* **281**, 137 (1989).
 - [10] J. Alarja, A. Dauchy, A. Giorni, C. Morand, E. Pollaco, P. Stassi, R. Billery, B. Chambon, B. Cheynis, D. Drain, and C. Pastor, *Nucl. Instrum. Methods Phys. Res. Sect. A* **242**, 352 (1986).
 - [11] I. Slypen, V. Corcalciuc, A. Ninane, and J. P. Meulders, *Nucl. Instrum. Methods Phys. Res. Sect. A* **337**, 431 (1994).
 - [12] I. Slypen, V. Corcalciuc, and J. P. Meulders, *Rom. J. Phys.* **38**, 419 (1993).
 - [13] A. Ninane, P. Duhamel, Y. Longree, M. Nemry, and F. Somers, *Proceedings of the Open Bus System '92, Zurich* (VFEA International, Trade Association ISBN 90-72577-11-6).
 - [14] I. Slypen, V. Corcalciuc, and J. P. Meulders, *Nucl. Instrum. Methods Phys. Res. Sect. B* **88**, 275 (1994).
 - [15] T. S. Subramanian, J. L. Romero, F. P. Brady, J. W. Watson, D. H. Fitzgerald, R. Garrett, G. A. Needham, J. L. Ullmann, C. I. Zanelli, D. J. Brenner, and R. E. Prael, *Phys. Rev. C* **28**, 521 (1983); J. L. Romero, private communication.
 - [16] D. J. Brenner and R. E. Prael, *At. Nucl. Data Tables* **41**, 71 (1989).
 - [17] K. Chen, Z. Fraenkel, G. Friedlander, J. R. Grover, J. M. Miller, and Y. Shimamoto, *Phys. Rev.* **166**, 949 (1968).
 - [18] G. J. Mathews, B. G. Glagola, R. A. Moyle, and V. E. Viola, Jr., *Phys. Rev. C* **25**, 2181 (1982).
 - [19] F. P. Brady, C. M. Castaneda, J. L. Ullmann, J. L. Romero, T. D. Ford, L. Johnson, N. S. P. King, C. M. Morris, F. Petrovich, and R. H. Howell, *Phys. Rev. Lett.* **48**, 860 (1982).
 - [20] F. P. Brady, T. D. Ford, G. A. Needham, J. L. Romero, D. S. Sorenson, C. M. Castaneda, J. L. Drummond, E. L. Hjort, B. McEachen, N. S. P. King, and D. J. Millener, *Phys. Rev. C* **43**, 2284 (1991).
 - [21] D. A. Kellogg, *Phys. Rev.* **90**, 224 (1953).
 - [22] I. Slypen, V. Corcalciuc, and J. P. Meulders, *Phys. Med. Biol.* **40**, 73 (1995).